Journal of Biomechanics 84 (2019) 18–26

Contents lists available at ScienceDirect

Journal of Biomechanics

journal homepage: www.elsevier.com/locate/jbiomech
www.JBiomech.com

# Biomechanical characterization of murine pulmonary arteries

Abhay B. Ramachandra [a], Jay D. Humphrey [a,b,*]

[a] Department of Biomedical Engineering, Yale University, New Haven, CT, United States
[b] Vascular Biology and Therapeutics Program, Yale School of Medicine, New Haven, CT, United States

ARTICLE INFO

*Article history:*
Accepted 5 December 2018

*Keywords:*
Pulmonary
Biaxial mechanics
Smooth muscle
Contractility
Mechanical stress

ABSTRACT

The biomechanical properties of the major pulmonary arteries play critical roles in normal physiology as well as in diverse pathophysiologies and clinical interventions. Importantly, advances in medical imaging enable simulations of pulmonary hemodynamics, but such models cannot reach their full potential until they are informed with region-specific material properties. In this paper, we present passive and active biaxial biomechanical data for the right and left main pulmonary arteries from wild-type mice. We also evaluate the suitability of a four-fiber family constitutive model as a descriptor of the passive behavior. Despite regional differences in size, the biaxial mechanical properties, including passive stiffness and elastic energy storage, the biaxial wall stresses at in vivo pressures, and the overall contractile capacity in response to smooth muscle cell stimulation under in vivo conditions are remarkably similar between the right and left branches. The proposed methods and results can serve as baseline protocols and measurements for future biaxial experiments on murine models of pulmonary pathologies, and the constitutive model can inform computational models of normal pulmonary growth and remodeling. Our use of consistent experimental protocols and data analyses can also facilitate comparative studies in health and disease across the systemic and pulmonary circulations as well as studies seeking to understand remodeling in surgeries such as the Fontan procedure, which involves different types of vessels.

## 1. Introduction

Pulmonary arteries are moderate-pressure, high-flow conduits. They remodel when exposed to altered biomechanical environments, as, for example, in chronic lung disease, congenital heart defects, hypertension, and valvular stenosis as well as in surgeries such as the Ross or Fontan procedures. Understanding such remodeling necessitates knowledge of the normal properties. Although we ultimately seek to understand the human condition, mouse models have become increasingly useful for understanding genetic, molecular, and mechanical mechanisms of arterial health and disease. While considerable effort has been directed towards biomechanically phenotyping systemic arteries in mice (e.g., Agianniotis and Stergiopulos, 2012; Bellini et al., 2017; Bersi et al., 2017; Ferruzzi et al., 2015; Le et al., 2014; Sutliff et al., 2014; Sutton et al., 2008), notwithstanding notable exceptions (e.g., Kobs et al., 2005; Wang and Chesler, 2012; Wang et al., 2013), there have been fewer studies of pulmonary arteries in mice, especially under biaxial loading conditions. The goal of this study, therefore, is to document active and passive biaxial biomechanical behaviors of the primary branch pulmonary arteries in mice using methods that are used for systemic arteries and veins. In this way, we provide novel data for pulmonary arteries that can be compared directly to nearby vessels such as the ascending aorta, carotid artery, and vena cava. Consistent experimental protocols involve similar handling and treatment, experimental protocols, constitutive equations, and methods of data analysis, including selection of the objective function and method of regression analysis. Such consistency promotes rigor and reproducibility and thereby facilitates comparative studies across vessels from different regions of circulation or having different pathologies (Bellini et al., 2017; Bersi et al., 2014; Ferruzzi et al., 2013). Indeed, having data and results derived from consistent methods is essential for designing and understanding surgeries such as the Fontan procedure, which involves different types of vessels.

## 2. Methods

All animal protocols were approved by the Institutional Animal Care and Use Committee of Yale University. Male mice (C57BL/6J from Jackson Labs, ME) between the ages of 14–20 weeks ($n = 14$) were euthanized with an intraperitoneal injection of

---

* Corresponding author at: Department of Biomedical Engineering, Yale University, New Haven, CT 06520, United States.

*E-mail address:* jay.humphrey@yale.edu (J.D. Humphrey).

https://doi.org/10.1016/j.jbiomech.2018.12.012
0021-9290/

Beuthanasia-D (150 mg/kg) followed by exsanguination. The pulmonary arteries were harvested from the main pulmonary artery to the first branch on the right (RPA) and left (LPA) pulmonary artery. Ten of the 14 excised vessels were prepared for biomechanical testing as described previously (Ferruzzi et al., 2013). Briefly, specimens were flushed of blood with a Hanks buffered physiologic solution consisting of (in mM): NaCl (138), KCl (5.3), $MgCl_2$-6 $H_2O$ (0.5), $MgSO_4$-7$H_2O$ (0.4), $NaHCO_3$ (4.2), $KH_2PO_4$ (0.4), $Na_2HPO_4$-anhyd (0.3), dextrose (5.6), and $CaCl_2$-anhyd (1.3) (Hanks and Wallace, 1949). Next, perivascular tissue and fat were gently removed, and small branch vessels were ligated with suture (left branch when right was tested and vice versa). Each vessel was then cannulated on custom glass micropipettes, beyond the main pulmonary artery, and secured with ligatures at the bifurcation of the main branch on one end and the first bifurcation of the branch pulmonary at the other end (Supplemental Fig. S1). The vessel was mounted in the biaxial testing device within a buffered Krebs-Ringer solution, consisting of (in mM) NaCl (123), KCl (4.7), $MgCl_2$ (1.2), $NaHCO_3$ (20), $KH_2PO_4$ (1.2), glucose (5.5), and $CaCl_2$ (2.5) and maintained at 37 °C and a pH of ~7.4 while bubbled with 95% $O_2$ and 5% $CO_2$ (Rahman et al., 2014).

### 2.1. Testing protocols

The specimens were tested using a custom computer-controlled testing device (Gleason et al., 2004), with an active protocol followed by a passive protocol ($n = 5$ each for RPA and LPA). Active testing was similar to protocols for systemic vessels (Caulk et al., 2018; Murtada et al., 2016) and focused predominantly on contractile responses close to in vivo conditions, that is, a mean distending pressure of 15 mmHg and the specimen-specific value of in vivo axial stretch. First, however, the smooth muscle cells were conditioned at 10 mmHg and an axial stretch of 1.1 (relative to the unloaded length) by contracting the vessel with 100 mM KCl. Axial stretch was subsequently increased in steps of 0.01 and pressure in steps of 1 mmHg to avoid sudden large deformations, which could compromise the viability of the smooth muscle. Following conditioning, the vessels were contracted with 100 mM KCl and then 1 μM phenylephrine (PE), both at 15 mmHg and the in vivo axial stretch. This protocol consisted of 5 min of equilibration, 15 min of contraction, and 10 min relaxation following washout of the vaso-stimulant with a fresh Krebs Ringer solution. Active testing was then followed by passive preconditioning (six cycles of inflation from 5 to 40 mmHg at the specimen-specific value of in vivo stretch), then two cycles of pressure-diameter tests (5–40 mmHg) at each of three different fixed axial stretches (95%, 100% and 105% of the in vivo axial stretch) and two cycles of force-length tests at each of four different pressures (5, 15, 25, and 40 mmHg) for a total of 7 protocols, all in Hanks buffered physiologic solution. Data from the final unloading curve of each protocol were used for analysis, consistent with prior studies. Vessel behavior in this Hanks-buffered solution containing lower calcium is nearly passive (Ferruzzi et al., 2011). Note, too, that in vivo stretch was determined by plotting transducer-measured axial force as a function of pressure at different values of axial stretch and finding that value at which axial force is independent of pressure (van Loon et al., 1977; Weizsäcker et al., 1983). Force and pressure were measured with standard transducers; diameter was measured with a video-microscope and custom software, and overall length was prescribed via sub-micron resolution stepper motors.

Vessels not used for mechanical testing were fixed in 10% neutral buffered formalin and stored in 70% ethanol at 4 °C for histology. Samples of the right and left pulmonary arteries, same sites tested mechanically, were embedded in paraffin, sectioned (5 μm thickness), and stained with Verhoeff's Van Giesen (VVG) or Masson's Trichrome (MTC) stains. Details of image quantification can be found elsewhere (Bersi et al., 2017). Briefly, each section was imaged with an Olympus BX/51 microscope using an Olympus DP70 digital camera under a 40× magnification objective. Complete cross-sections were obtained by stitching together sub-images with Image Composite Editor software (Microsoft Research). The stitched images were subsequently analyzed using custom MATLAB scripts. Briefly, following background subtraction and pixel-based thresholding, area fractions for elastin (from VVG) and cytoplasm (from MTC) were computed as the ratio of pixels corresponding to a stain divided by the total number of pixels in the image. Because MTC can overstain collagen, its area fraction was computed as 1 - area fraction of elastin plus cytoplasm, while assuming that GAG content was negligible (Ferruzzi et al., 2015, 2018), as confirmed with Movat Pentachrome staining (data not shown). Three sections were analyzed per vessel per stain.

### 2.2. Data analysis

We used a 2-D formulation to model the passive behavior since residual stresses in normal arteries tend to homogenize the stress field, thereby rendering mean values as good estimates of overall wall stress (Humphrey, 2013). Mean values of the in-plane components of Cauchy stress across the wall (i.e., neglecting radial stresses) are estimated as

$$\sigma_\theta^{exp} = \frac{Pr_i}{r_o - r_i}, \quad \text{and} \quad \sigma_z^{exp} = \frac{f_T + P\pi r_i^2}{\pi(r_o^2 - r_i^2)}, \tag{1}$$

where $P$ is the transmural pressure, $r_i$ the internal radius, $r_o$ the outer radius, and $f_T$ the axial force measured by the force transducer; subscripts θ and $z$ refer to circumferential and axial directions, respectively. Inner radius and wall thickness, $h$, are computed from measured quantities, assuming incompressibility, as

$$r_i = \sqrt{r_o^2 - \bar{V}/\pi l}, \quad \text{and} \quad h = r_o - r_i, \tag{2}$$

where $l$ is the instantaneous length between the ligatures securing the vessel to the micropipettes and $\bar{V} = \frac{\pi}{4}L(OD^2 - ID^2)$ is the volume of the vessel in the unloaded state, where $L$ is the unloaded length, $OD$ the unloaded outer diameter, and $ID = OD - 2H$ the unloaded inner diameter with $H$ the unloaded thickness. Mean stretch ratios are calculated as $\lambda_\theta = r_{mid}/\rho_{mid}$, $\lambda_z = l/L$ and, using incompressibility, $\lambda_r = 1/\lambda_\theta\lambda_z$, where $r_{mid} = (r_i + r_o)/2$ and $\rho_{mid}$ are the loaded and unloaded mid-wall radius, respectively.

The nonlinear passive behavior is modeled using a pseudoelastic constitutive framework in terms of a scalar stored energy function, $W$. Stress and material stiffness can be computed from first and second derivatives of $W$ with respect to an appropriate measure of deformation (Ferruzzi et al., 2013). This constitutive relation has successfully described the passive biaxial behavior of systemic arteries and veins from mice (Ferruzzi et al., 2013; Lee et al., 2013; Schroeder et al., 2018; Zeinali-Davarani et al., 2009) and using the same form here facilitates inter-vessel comparisons. Hence, let

$$W = \frac{c}{2}(I_c - 3) + \sum_{i=1}^{4} \frac{c_1^i}{4c_2^i}\left\{exp\left[c_2^i\left(IV_c^i - 1\right)^2\right] - 1\right\} \tag{3}$$

where $c$, $c_1^i$ and $c_2^i$ are material parameters to be determined by nonlinear regression; $i = 1,2,3,4$ represent four families of locally parallel fibers along axial, circumferential, and two symmetric diagonal directions, respectively. $I_c$ is the first invariant of right Cauchy-Green tensor and $IV_c^i$ is the square of the stretch of the $i^{th}$ fiber family, namely, $IV_c^i = \lambda_\theta^2 \sin^2 \alpha_0^i + \lambda_z^2 \cos^2 \alpha_0^i$, where $\alpha_0^i$ is the fiber angle relative to axial direction in the reference configuration.

Best-fit values of the eight model parameters ($c$, $c_1^1$, $c_2^1$, $c_1^2$, $c_2^2$, $c_1^{3,4}$, $c_2^{3,4}$ and $\alpha_0^i$) were obtained by minimizing the objective function (using *lsqnonlin* in Matlab with a *trust-region-reflective* option, tolerance = 1e-10)

$$J = \sum_{i=1}^{N}\left[\left(\frac{P^{th} - P^{exp}}{\bar{P}^{exp}}\right)_i^2 + \left(\frac{f^{th} - f^{exp}}{\bar{f}^{exp}}\right)_i^2\right] \tag{4}$$

where $N$ is the number of equilibrium states (hundreds when combining data from seven protocols), *th* denotes theoretically computed, exp denotes experimentally measured, and an overbar denotes a mean value. Bounds for the parameters [$c$, $c_1^1$, $c_2^1$, $c_1^2$, $c_2^2$, $c_1^{3,4}$, $c_2^{3,4}$, $\alpha_0^i$] were [0, 0, 1e-6, 0, 1e-6, 0, 1e-6, 0] and [1e5, 1e5, 1e5, 1e5, 1e5, 1e5, 1e5, 90°], similar to those used previously (Bersi et al., 2017; Ferruzzi et al., 2013; Lee et al., 2013), and converged parameters were confirmed using three random sets of initial guesses.

Although best-fit values of material parameters are central to constitutive modeling, comparisons between the RPA and LPA focused on geometric and mechanical quantities, including biaxial stress and material stiffness as well as elastic energy storage. Such mechanical quantities are much less sensitive to the non-uniqueness of parameter values inherent to exponential models. We used the theory of "small deformations superimposed on large" to compute a linearized material stiffness appropriate over a cardiac cycle, again consistent with previous work and motivated by the desire to inform fluid-solid-interaction models (cf. Figueroa et al., 2009). Associated calculations thus follow our previous work (Baek et al., 2007; Bersi et al., 2017; Ferruzzi et al., 2013). To facilitate additional comparisons with some prior reports in the literature, we also computed distensibility

$$D = \frac{d_{sys} - d_{dias}}{d_{dias}(P_{sys} - P_{dias})} \tag{5}$$

where subscripts *sys* (~25 mmHg) and *dias* (~10 mmHg) denote systole and diastole, respectively, and $d$ denotes outer diameter.

### 2.3. Statistics

A one-way ANOVA with Tukeys post-hoc analysis assessed potential statistical differences in morphological, mechanical, and contractile properties between RPA and LPA.

## 3. Results

Mean pressure-diameter, axial force-stretch, and biaxial Cauchy stress-stretch behaviors are compared in Fig. 1 for RPAs and LPAs ($n$ = 5 per group); the pressure-diameter data are shown for individual in vivo values of axial stretch and the force-stretch data are shown at a common mean pressure (15 mmHg). Both the pressure-diameter and force-stretch curves are qualitatively similar to those for systemic arteries (Ferruzzi et al., 2013, 2015), though strain-stiffening occurs at much lower values of pressure and axial force. The structural behaviors differ slightly for the RPA and LPA, but these differences appear to arise primarily because of the different sizes (Table 1 and Supplemental Table S1), thus the associated material behaviors appear similar.

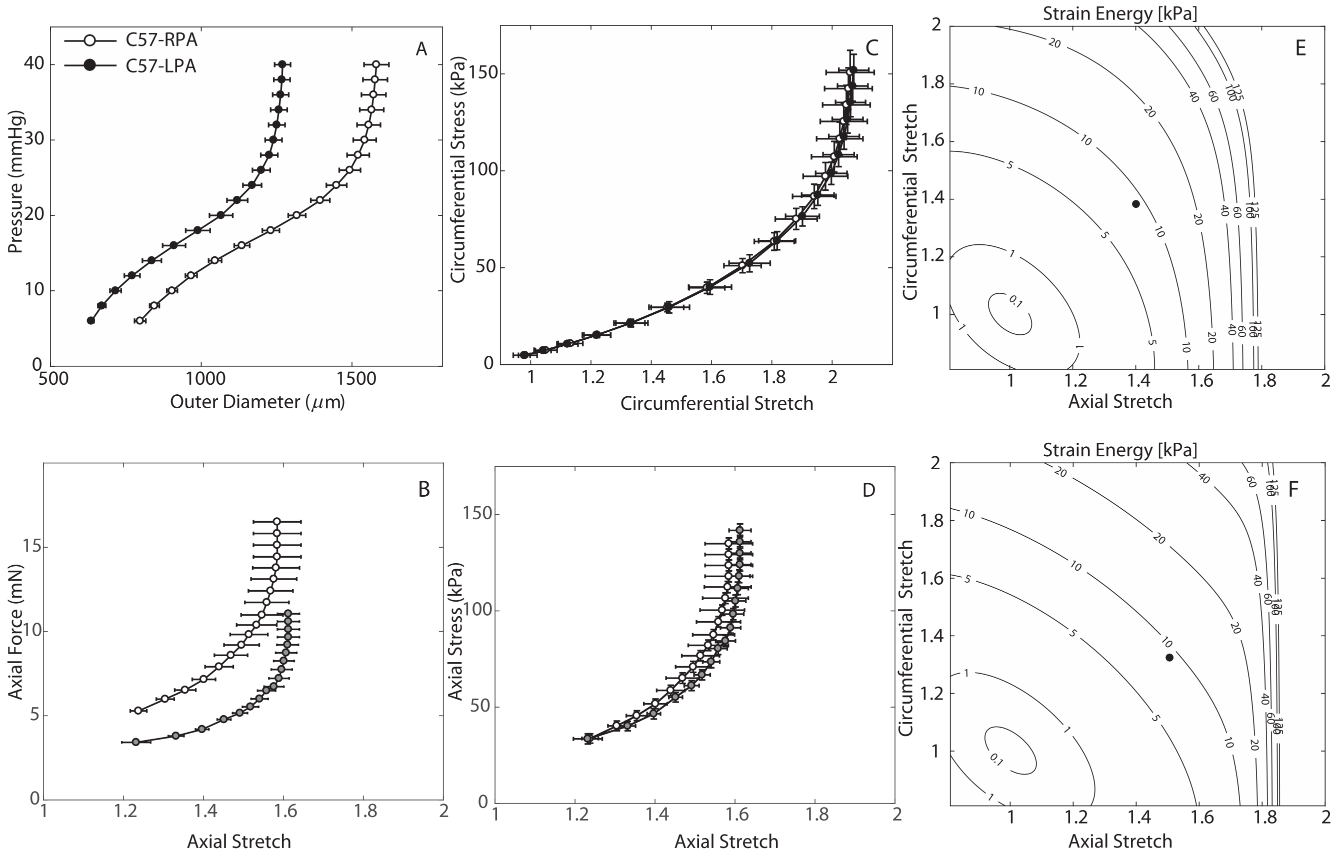

**Fig. 1.** Mechanical behavior of right (RPA – open circles) and left (LPA – filled circles) pulmonary arteries from C57BL/6J mice ($n$ = 5 per group): pressure-diameter (A) and axial force-stretch (B) behaviors and associated circumferential (C) and axial (D) Cauchy stress – stretch behaviors, all at vessel-specific values of in vivo axial stretch (Mean ± SEM). Shown, too, are representative iso-energy contours for RPA (E) and LPA (F), with the filled symbol representing elastic stored energy at a common mean pressure of 15 mmHg but vessel-specific in vivo stretch. Although RPA and LPA exhibit different structural behaviors (A & B), they have similar material behaviors (C & D).

**Table 1**
Unloaded length, diameter, and thickness for samples from the right (RPA) and left (LPA) pulmonary arteries from adult male C57BL/6 mice.

| Type | | Unloaded length (mm) | Unloaded diameter($\mu$m) | Unloaded thickness ($\mu$m) |
|---|---|---|---|---|
| Right pulmonary artery | RPA1 | 2.98 | 867 | 81 |
| | RPA2 | 3.06 | 769 | 79 |
| | RPA3 | 4.08 | 843 | 76 |
| | RPA4 | 2.62 | 817 | 83 |
| | RPA5 | 2.81 | 886 | 90 |
| | Mean ± SD | 3.11 ± 0.57 | 836 ± 46 | 82 ± 5 |
| Left pulmonary artery | LPA1 | 3.47 | 671 | 61 |
| | LPA2 | 3.37 | 669 | 69 |
| | LPA3 | 3.28 | 676 | 69 |
| | LPA4 | 3.67 | 646 | 68 |
| | LPA5 | 3.77 | 682 | 66 |
| | Mean ± SD | 3.51 ± 0.20 | 669 ± 14 | 66 ± 3 |

**Table 2**
Best-fit values of model parameters for the so-called four-fiber family model with a neo-Hookean relation capturing collective isotropic contributions to material behavior (mainly elastin) and Fung-type exponential relations capturing collective anisotropic contributions (mainly collagen fibers and passive smooth muscle); see Eq. (3). Results listed for $n = 5$ right (RPA) and left (LPA) pulmonary arteries in the passive state. Note that mean values need not be representative of the average mechanical behavior (see Supplementary Table S2 and Supplementary Fig. S2).

| Type | | Elastic fibers | Axial collagen | | Circumferential collagen + smooth muscle cell | | Diagonal collagen | | | |
|---|---|---|---|---|---|---|---|---|---|---|
| | | $c$ (kPa) | $c_1^1$ (kPa) | $c_2^1(-)$ | $c_1^2$ (kPa) | $c_2^2$ (−) | $c_1^{3,4}$ (kPa) | $c_2^{3,4}$ (−) | $\alpha_0$(deg) | RMSE |
| Right pulmonary artery | RPA1 | 10.483 | 1.997 | 1.075 | 3.1e−4 | 0.772 | 4.181 | 0.393 | 38.698 | 0.106 |
| | RPA2 | 6.472 | 4.172 | 0.636 | 1.903 | 1e−6 | 1.816 | 0.534 | 31.600 | 0.090 |
| | RPA3 | 12.026 | 2.339 | 1.113 | 0.669 | 0.248 | 1.318 | 1.138 | 36.506 | 0.093 |
| | RPA4 | 10.800 | 1.858 | 0.184 | 0.290 | 0.144 | 2.032 | 0.293 | 40.824 | 0.086 |
| | RPA5 | 9.857 | 0.133 | 0.903 | 2.9e−5 | 0.897 | 1.993 | 0.366 | 42.028 | 0.089 |
| | Mean ± SD | 9.928 ± 2.087 | 2.100 ± 1.439 | 0.782 ± 0.384 | 0.573 ± 0.793 | 0.412 ± 0.398 | 2.268 ± 1.107 | 0.545 ± 0.343 | 37.9 ± 4.1 | 0.093 ± 0.008 |
| Left pulmonary artery | LPA1 | 9.167 | 0.006 | 1.984 | 0.648 | 1e−6 | 5.030 | 0.262 | 42.143 | 0.141 |
| | LPA2 | 11.633 | 0.162 | 0.892 | 0.356 | 0.212 | 0.943 | 0.538 | 38.511 | 0.092 |
| | LPA3 | 8.790 | 0.089 | 2.141 | 1.467 | 1e−6 | 2.827 | 0.549 | 38.205 | 0.125 |
| | LPA4 | 6.669 | 4.327 | 0.316 | 1.468 | 1e−6 | 1.140 | 0.402 | 37.207 | 0.101 |
| | LPA5 | 10.787 | 0.151 | 1.553 | 0.406 | 0.142 | 1.201 | 0.602 | 34.794 | 0.081 |
| | Mean ± SD | 9.409 ± 1.923 | 0.947 ± 1.890 | 1.377 ± 0.765 | 0.869 ± 0.557 | 0.071 ± 0.100 | 2.228 ± 1.739 | 0.471 ± 0.138 | 38.2 ± 2.7 | 0.108 ± 0.025 |

Best-fit values of the eight material properties in the four-fiber family constitutive relation are listed in Table 2 for all 10 vessels tested. The fit to the passive biaxial data was good for both the RPA and the LPA (see Supplemental Fig. S3), similar to fits to data for systemic arteries (Bellini et al., 2017; Bersi et al., 2017; Ferruzzi et al., 2015). With this constitutive relation, we calculated multiple mechanical metrics of interest, including elastically stored energy (Fig. 1). Values of stored energy on the order of 10 kPa are much less than that for a common elastic artery such as the thoracic aorta (on the order of 100 kPa in the mouse (Jiao et al., 2017)). Passive morphological and mechanical metrics are summarized in Fig. 2 for both branches at in vivo conditions. The unloaded and loaded (at 25 mmHg) diameter and similarly unloaded and loaded wall thickness are significantly different between the RPA and LPA. Again, however, none of the intrinsically normalized mechanical metrics, including strain energy density and biaxial Cauchy stress and stiffness, are significantly different between the right and left branches. Indeed, even the common clinical metric of compliance, $D$, is similar between the RPA and LPA.

Active contractile responses, at a fixed pressure (15 mmHg) and specimen-specific axial stretch, are summarized in Figs. 3 and 4 for KCl- and PE-induced contractions of both RPAs and LPAs. The former shows Mean ± SEM temporal changes in outer diameter, normalized by the basal outer diameter at 15 mmHg and individual values of in vivo axial stretch. Consistent with these findings, Fig. 4 shows that the only statistical differences between RPA and LPA is again size. That is, percent vaso-stimulant induced diameter reduction and stress reduction are similar between the two branches. Importantly, the normalized change in outer diameter is ~25 to 30% at 15 min (Fig. 3), ~7 to 12% more than that in the ascending aorta in the corresponding genotype (unpublished data).

Representative Verheoff-van Gieson (VVG) and Masson's Trichrome (MTC) sections are shown in Fig. 5 for the RPA and LPA. As it can be seen, both branches have similar area fractions of elastin (0.249 ± 0.072 vs. 0.255 ± 0.081), cytoplasm (0.215 ± 0.045 vs. 0.180 ± 0.051), and collagen (0.536 ± 0.106 vs. 0.565 ± 0.122). As expected, the number of elastic laminae is less than for nearby intrathoracic systemic arteries such as the aorta (Bersi et al., 2017).

## 4. Discussion

Prior studies of the biomechanical properties of pulmonary arteries, particularly in rodents, have yielded considerable insight into structure-function relations in health and disease. For example, Kobs et al. (2005) report an increase in an 'effective' circumferential stiffness in the mouse LPA due to hypoxia. Pursell et al. (2016) similarly report an increase in a circumferential modulus in the rat RPA in a monocrotaline-induced model of pulmonary artery hypertension, though the axial modulus decreased at early (1 week) and then increased at advanced (4 weeks) hypertension. Huang et al. (2001) report values of circumferential, axial, and cross incremental moduli for normal and hypoxic LPA in a rat. Despite differences in protocols, definitions, and species, our values of linearized circumferential stiffness in healthy mice LPA at mean (98 ± 12 kPa) and systolic (430 ± 48 kPa) pressures bound the previously reported values (e.g., 171 ± 13 kPa (Huang et al., 2001);

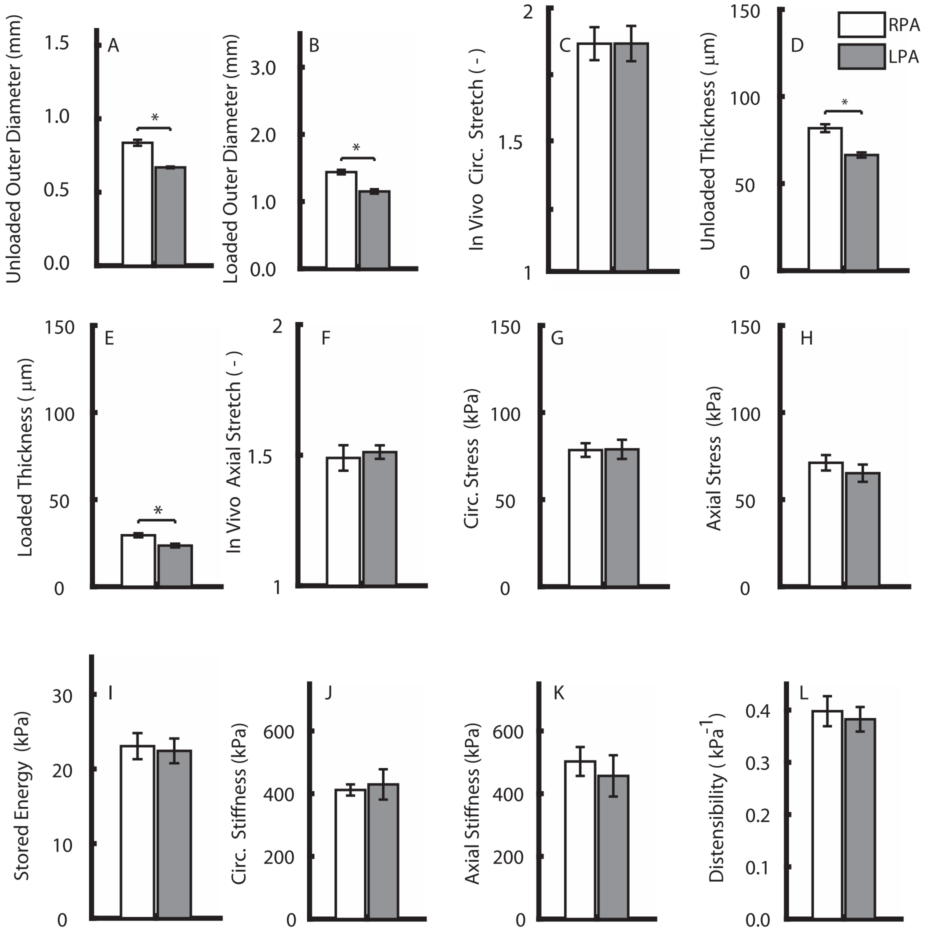

**Fig. 2.** Comparison of morphological and mechanical metrics for right (RPA, white, $n = 5$) and left (LPA, grey, $n = 5$) pulmonary arteries from passive tests. Loaded dimensions (B, E), stored energy (I), biaxial Cauchy stress (G, H), and biaxial material stiffness (J, K) are reported for a systolic pressure of 25 mmHg and individual values of the in vivo axial stretch. * $p < 0.05$.

222 ± 35 kPa (Kobs et al., 2005)). Our value for the linearized axial stiffness (243 ± 38 at mean and 457 ± 66 at systolic pressure) is higher, however, than the value of 76.5 ± 31.1 kPa reported in Huang et al. (2001), where we note that axial stiffness is generally higher than or equal to that in the circumferential direction in systemic arteries but that sufficient axial information is needed for a good assessment. We do not compare our results with those of Pursell et al. (2016) since they used quasi-linear viscoelasticity and we used pseudoelasticity to analyze the data. Indeed, we purposely kept all our methods, protocols, and methods of data analysis consistent with those we have used for murine systemic arteries to facilitate future comparisons across circulations.

The values of in vivo axial stretch reported here for adult C57BL/6J male mice ($\lambda_z^{iv} \sim 1.49 \pm 0.05$ for RPA and $1.51 \pm 0.03$ for LPA) are similar to values reported previously ($\lambda_z^{iv} = 1.66$), albeit for rat pulmonary arteries (Huang et al., 2001). Our measured ratio of inner diameters for the RPA: LPA imply a flow split of 67%: 33% for a Poiseuille flow and assumption of a constant mean shear stress; this split is also close to the invasive measurement of a 68%: 32% split in rat pulmonary arteries (Razavi et al., 2011). It thus appears that the significant difference in diameters between the RPA and LPA is governed largely by flow (cf. Dajnowiec and Langille, 2007). Nevertheless, the murine RPA and LPA have similar material properties in health (Figs. 1, 2, and 4). In contrast, multiple studies have observed regional differences in mechanical properties between the right and left pulmonary branches in rats in pulmonary hypertension (Drexler et al., 2008; Pursell et al., 2016). Identifying reasons for this differential mechano-adaptive response could be important in determining differential disease propensity. Towards that end, linking mechanical and biological aspects of remodeling will be critical, and histology and immunohistochemical assays will play key roles (Humbert et al., 2004; Kobs et al., 2005). Notwithstanding possible differences due to age, 14–20 weeks herein and 6 weeks in Kobs et al. (2005), our quantified levels of elastin (RPA = 0.249 ± 0.072 and LPA = 0.255 ± 0.081 vs. 0.29 ± 0.03) and collagen (RPA = 0.536 ± 0.106 and LPA = 0.565 ± 0.122 vs. 0.46 ± 0.05) in health compared well with this prior study.

Although mechanisms underlying pulmonary remodeling are multifactorial, smooth muscle plays a central role (Fagan et al., 2004; Homma et al., 2007; Humbert et al., 2004; Siehr et al., 2016; Stenmark and McMurtry, 2005), especially during early periods of hypertension. Note, therefore, that plasma concentrations of endothelins are elevated in pulmonary hypertension in congenital heart patients (Yoshibayashi et al., 1991) and chronic prostacyclin improves hemodynamics and quality of life in those who fail conventional therapy (Rosenzweig et al., 1999). Multiple cell types, including endothelial and smooth muscle, are thus likely critical in pulmonary remodeling. Vaso-stimulants can activate different, and at times multiple, pathways of smooth muscle contraction or relaxation, and monocrotaline models of pulmonary hypertension in rats exhibit altered smooth muscle responsiveness (Altiere et al., 1986). Such alterations in vasoactivity could in turn influence microstructural changes (Langleben et al., 1988; Valentín et al.,

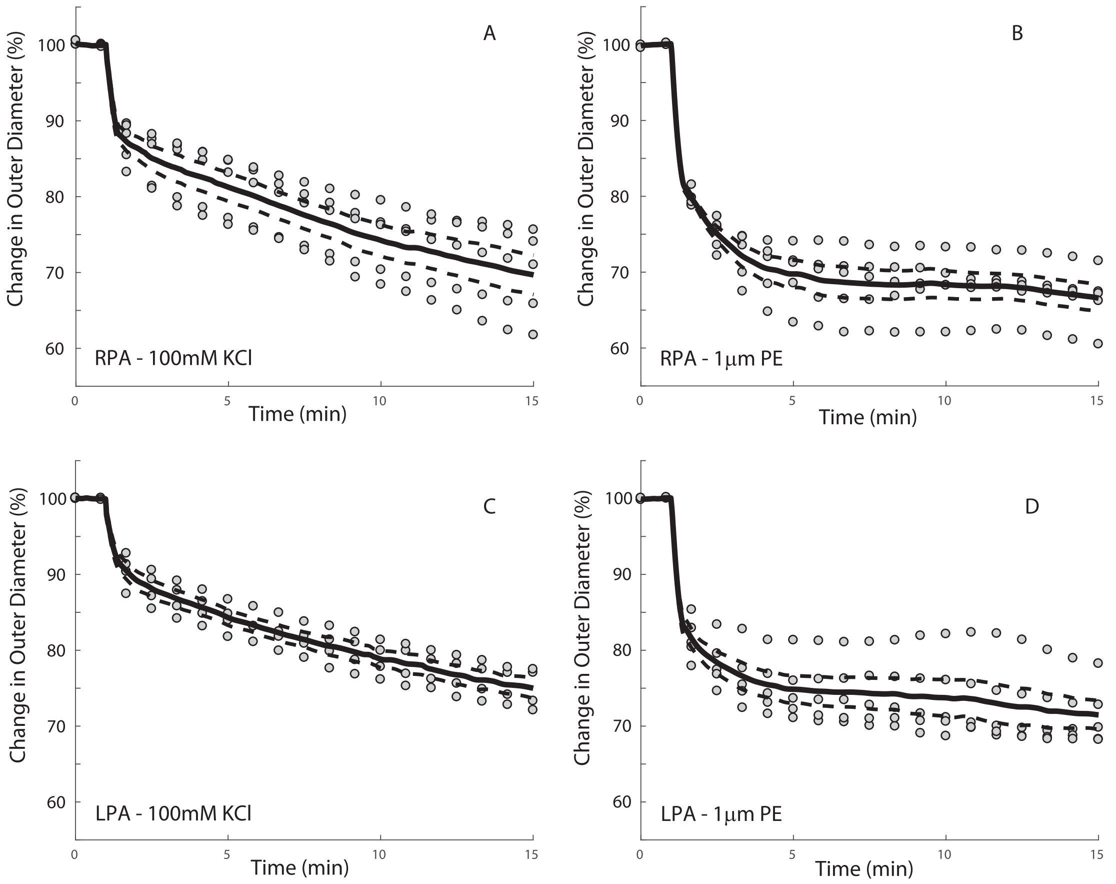

**Fig. 3.** Temporal change in outer diameter due to contraction of right (A, B; $n = 5$ each) and left (C, D; $n = 4$ for KCl, and $n = 5$ for PE) pulmonary arteries for 100 mM potassium chloride (KCl, A, C) and 1 μM phenylephrine (PE, B, D). Change in diameter is computed with respect to, and normalized against, outer diameter at vessel-specific in vivo axial stretch but a common mean pressure of 15 mmHg. Mean (solid line) ± SEM (dashed) overlaid on true data (solid circles) for different samples in each group.

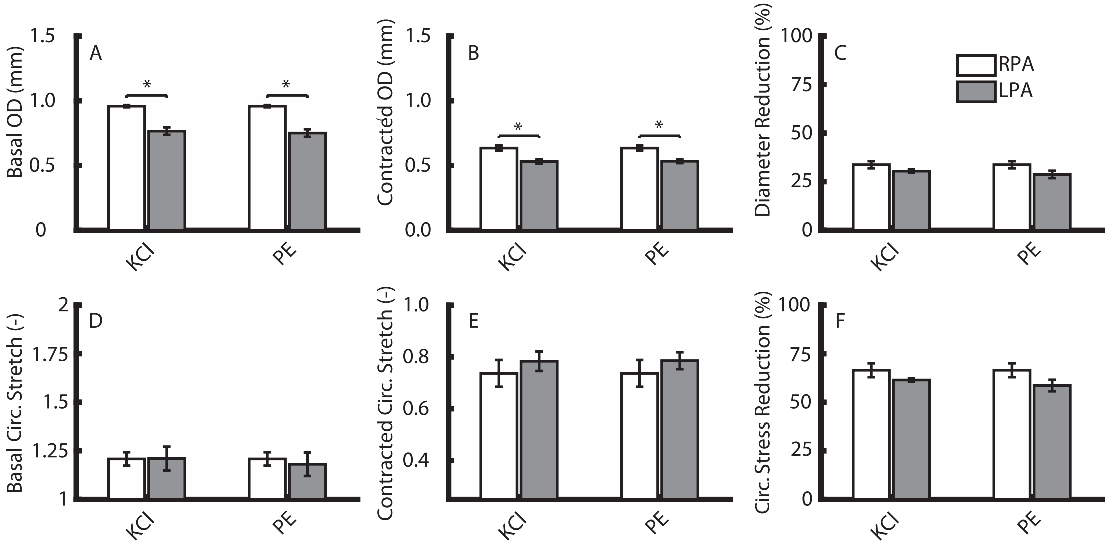

**Fig. 4.** Comparison of morphological and mechanical metrics for right (RPA, white) and left (LPA, grey) pulmonary arteries for active testing in response to 100 mM potassium chloride (KCl) ($n = 5$ for RPA and $n = 4$ for LPA) or 1 μM PE ($n = 5$ for RPA and LPA). Basal and contracted values are at a pressure of 15 mmHg and in vivo stretch. * $p < 0.05$.

2009). Hence it is important to study smooth muscle responses in a physiologically relevant setting. Uniaxial ring tests are useful for evaluating smooth muscle contraction, but they cannot account for any compensatory axial changes (Humphrey et al., 2009), they cannot separate finite stretching from bending (Humphrey, 2013), and they expose the intima, adventitia, and cut surfaces of the media to the stimulant directly, thus rendering the response less physiological. Not unexpectedly, therefore, sensitivity to vasostimulants is different in uniaxial isometric tests and biaxial isobaric tests (Caulk et al., 2018), with the latter more physiologically

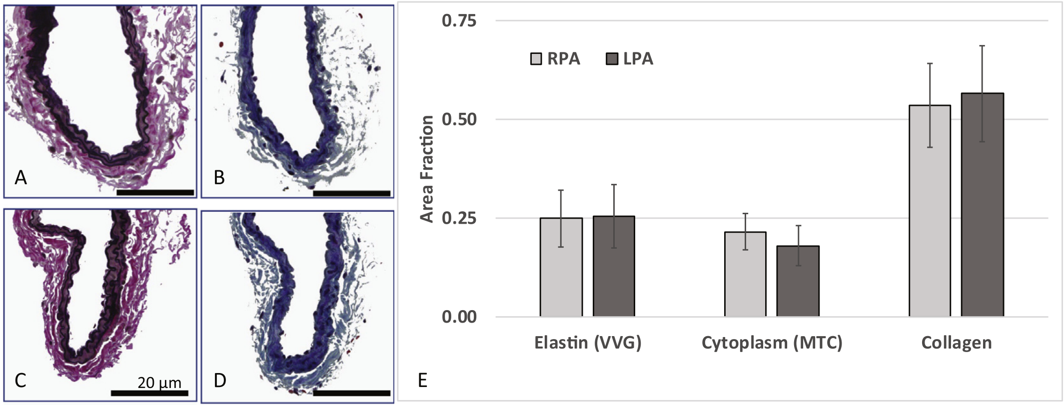

**Fig. 5.** Representative Verheoff-Van Gieson (VVG – left) and Masson's Trichrome (MTC – right) stained sections for a representative RPA (A and B, respectively) and LPA (C and D, respectively). Elastin appears black in VVG and connective tissue (mainly collagen) appears blue in MTC. The area fractions for elastin and cytoplasm (red in MTC) were computed based on $n = 12$ sections for each stain, with collagen calculated as 1- area fraction of elastin and cytoplasm. We assume GAG content in the wall is negligible (confirmed using a Movat Pentachrome stain, data not shown). (For interpretation of the references to colour in this figure legend, the reader is referred to the web version of this article.)

relevant. Thus, we measured vasoconstriction under physiologic pressure and axial stretch in response to KCl, which depolarizes the smooth muscle cell membrane and increases intracellular calcium, and PE, an alpha-adrenergic receptor agonist. Although neither the percent change in diameter nor the contractile stress was significantly different between healthy RPA and LPA for either stimulant, these contractile responses could differ in cases of disease and thereby influence the aforementioned differential remodeling in hypertension (Langleben et al., 1988). The reported data promise to serve as a baseline comparator for future studies of different pulmonary conditions as well as when exploring vasoactive pathways and promising drug therapies.

Multi-modal imaging has enabled mouse-specific simulations in genetically altered or pharmacologically treated mice (Phillips et al., 2017; Qureshi et al., 2018). Values of biaxial material stiffness reported herein can be used to inform such simulations (Cuomo et al., 2018), including those focused on growth (changes in mass) and remodeling (changes in microstructure). Whereas such models have made inroads into modeling the systemic and venous circulations in health and disease (Ramachandra et al., 2017; Valentín et al., 2009), models of pulmonary growth and remodeling remain few. Whereas our data and results on the four-fiber family constitutive model can inform computational models directly, there remains a need to formulate associated biaxial constitutive relations for active responses (Murtada et al., 2017), which will require additional testing protocols (Murtada et al., 2016). Our goal here was simply to qualitatively assess contractile capacity under in vivo conditions and to compare results from RPA and LPA.

In addition to the need for biaxial constitutive relations for the active behavior, which will require dose response data, there are other limitations of our study. First, the passive biaxial data could be fit equally well with other constitutive models, including other fiber family models (see Supplementary Tables S3 and S4 and Fig. S4). The four-fiber family model was previously shown to best-fit large systemic artery data (Baek et al., 2007; Ferruzzi et al., 2011) and thus was chosen herein to enable a consistent comparison with results from studies of systemic arteries (Bellini et al., 2017; Bersi et al., 2016; Eberth et al., 2009; Ferruzzi et al., 2015). As with all exponential models, the constitutive parameters in the four-fiber family model are inter-related, not unique, which can lead to variability of the estimated values (Table 2, see mean ± SD). We suggest, therefore, that it is prudent to interpret and compare biaxial results in terms of quantities such as stress, material stiffness, and stored energy rather than in terms of the phenomenological constitutive parameters (Table S4). Much more data, especially on the organization of the microstructure, will be needed to formulate truly structural models. Second, related to this issue, it is not possible to correlate standard histological observations with the best-fit values of the constitutive parameters, except possibly for the elastin parameter in a few select cases (Eberth et al., 2009). This limitation is common, of course, to all other current constitutive models for blood vessels. Histological data thus provide complementary information. Third, although care was taken to cannulate past the bifurcation of the LPA and RPA, it is difficult to avoid any contribution from the main PA as the pulmonary arteries branch at a steep angle, thus a short segment of the main PA could have contributed to the observed mechanical behavior, mainly in the axial direction.

Gaining insights into pulmonary pathologies, which are typically multifactorial with coupled mechanical and biological responses, requires an integrative approach. Thus, it is critical that experiments be designed not only with the aim of exploring pathological mechanisms but also with the aim of informing and furthering computational models, which then can guide the design of experiments and aid translation. While the quest for the right preclinical representative model of pulmonary hypertension or congenital heart disease remains (Gomez-Arroyo et al., 2011; Stenmark et al., 2009), mouse models still promise the advantage of being genetically modifiable and enabling detailed longitudinal studies (Hocher et al., 2000; Tojais et al., 2017; Wang and Chesler, 2012). Thus, our quantification of murine biomechanical properties, in a physiologically relevant setting, should serve as valuable baseline data for adult male wild-type (C57BL/6) controls to which other mouse models can be compared in future. Quantifying biomechanical properties in diseased genotypes will be a natural progression of this work. Future efforts should also be dedicated towards integrating data from these experiments into computational models.

## Acknowledgments

We thank Drs. A. Caulk and S-I. Murtada for guidance on active biaxial testing, Drs. A. Korneva, and B. Spronck for further technical assistance, and Drs. M. Bersi, J. Ferruzzi and R. Khosravi for valuable input on histology. This work was funded in part by NIH grants R01 HL 128602 and R01 HL 139796.

## Conflict of interest statement

All authors declare no conflict of interest

## Appendix A. Supplementary material

Supplementary data to this article can be found online at https://doi.org/10.1016/j.jbiomech.2018.12.012.

## References

Agianniotis, A., Stergiopulos, N., 2012. Wall properties of the apolipoprotein E-deficient mouse aorta. Atherosclerosis 223, 314–320.

Altiere, R.J., Olson, J.W., Gillespie, M., 1986. Altered pulmonary vascular smooth muscle responsiveness in monocrotaline-induced pulmonary hypertension. J. Pharmacol. Exp. Ther. 236, 390–395.

Baek, S., Gleason, R., Rajagopal, K., Humphrey, J., 2007. Theory of small on large: potential utility in computations of fluid–solid interactions in arteries. Comput. Meth. Appl. Mech. Eng. 196, 3070–3078.

Bellini, C., Bersi, M., Caulk, A., Ferruzzi, J., Milewicz, D., Ramirez, F., Rifkin, D., Tellides, G., Yanagisawa, H., Humphrey, J., 2017. Comparison of 10 murine models reveals a distinct biomechanical phenotype in thoracic aortic aneurysms. J. R. Soc. Interface 14, 20161036.

Bersi, M., Ferruzzi, J., Eberth, J., Gleason, R., Humphrey, J., 2014. Consistent biomechanical phenotyping of common carotid arteries from seven genetic, pharmacological, and surgical mouse models. Ann. Biomed. Eng. 42, 1207–1223.

Bersi, M., Khosravi, R., Wujciak, A., Harrison, D., Humphrey, J., 2017. Differential cell-matrix mechanoadaptations and inflammation drive regional propensities to aortic fibrosis, aneurysm or dissection in hypertension. J. R. Soc. Interface 14, 20170327.

Bersi, M.R., Bellini, C., Wu, J., Montaniel, K.R., Harrison, D.G., Humphrey, J.D., 2016. Excessive adventitial remodeling leads to early aortic maladaptation in angiotensin-induced hypertension. Hypertension 67 (5), 890–896. https://doi.org/10.1161/HYPERTENSIONAHA.115.06262.

Caulk, A., Humphrey, J.D., Murtada, S.-I., 2018. Fundamental roles of axial stretch in isometric and isotonic evaluations of vascular contractility. J. Biomech. Eng. https://doi.org/10.1115/1.4042171 (accepted for publication).

Cuomo, F., Ferruzzi, J., Li, C., Zhuang, Z., Humphrey, J., Figueroa, C.A., 2018. Sex-dependent differences in central artery hemodynamics in normal and fibulin-5 deficient mice: implications for aging (Proc R Soc A 20180076, accepted in Proc of R Soc A).

Dajnowiec, D., Langille, B.L., 2007. Arterial adaptations to chronic changes in haemodynamic function: coupling vasomotor tone to structural remodelling. Clin. Sci. 113, 15–23.

Drexler, E.S., Bischoff, J., Slifka, A., McCowan, C., Quinn, T.P., Shandas, R., Ivy, D., Stenmark, K., 2008. Stiffening of the extrapulmonary arteries from rats in chronic hypoxic pulmonary hypertension. J. Res. Nat. Inst. Stand. Technol. 113, 239.

Eberth, J., Taucer, A., Wilson, E., Humphrey, J., 2009. Mechanics of carotid arteries in a mouse model of Marfan syndrome. Ann. Biomed. Eng. 37, 1093–1104.

Fagan, K.A., Oka, M., Bauer, N.R., Gebb, S.A., Ivy, D.D., Morris, K.G., McMurtry, I.F., 2004. Attenuation of acute hypoxic pulmonary vasoconstriction and hypoxic pulmonary hypertension in mice by inhibition of Rho-kinase. Am. J. Physiol.-Lung Cellular Mol. Physiol. 287, L656–L664.

Ferruzzi, J., Bersi, M., Humphrey, J., 2013. Biomechanical phenotyping of central arteries in health and disease: advantages of and methods for murine models. Ann. Biomed. Eng. 41, 1311–1330.

Ferruzzi, J., Bersi, M., Uman, S., Yanagisawa, H., Humphrey, J., 2015. Decreased elastic energy storage, not increased material stiffness, characterizes central artery dysfunction in fibulin-5 deficiency independent of sex. J. Biomech. Eng. 137, 031007.

Ferruzzi, J., Collins, M.J., Yeh, A.T., Humphrey, J.D., 2011. Mechanical assessment of elastin integrity in fibrillin-1-deficient carotid arteries: implications for Marfan syndrome. Cardiovasc. Res. 92, 287–295.

Ferruzzi, J., Madziva, D., Caulk, A., Tellides, G., Humphrey, J., 2018. Compromised mechanical homeostasis in arterial aging and associated cardiovascular consequences. Biomech. Model. Mechanobiol., 1–15

Figueroa, C.A., Baek, S., Taylor, C.A., Humphrey, J.D., 2009. A computational framework for fluid–solid-growth modeling in cardiovascular simulations. Comput. Meth. Appl. Mech. Eng. 198, 3583–3602.

Gleason, R., Gray, S., Wilson, E., Humphrey, J., 2004. A multiaxial computer-controlled organ culture and biomechanical device for mouse carotid arteries. J. Biomech. Eng. 126, 787–795.

Gomez-Arroyo, J.G., Farkas, L., Alhussaini, A.A., Farkas, D., Kraskauskas, D., Voelkel, N.F., Bogaard, H.J., 2011. The monocrotaline model of pulmonary hypertension in perspective. Am. J. Physiol.-Lung Cellular Mol. Physiol. 302, L363–L369.

Hanks, J.H., Wallace, R.E., 1949. Relation of oxygen and temperature in the preservation of tissues by refrigeration. Proc. Soc. Exp. Biol. Med. 71, 196–200.

Hocher, B., Schwarz, A., Fagan, K.A., Thone-Reineke, C., El-Hag, K., Kusserow, H., Elitok, S., Bauer, C., Neumayer, H.-H., Rodman, D.M., 2000. Pulmonary fibrosis and chronic lung inflammation in ET-1 transgenic mice. Am. J. Respir. Cell Mol. Biol. 23, 19–26.

Homma, N., Nagaoka, T., Morio, Y., Ota, H., Gebb, S.A., Karoor, V., McMurtry, I.F., Oka, M., 2007. Endothelin-1 and serotonin are involved in activation of RhoA/Rho kinase signaling in the chronically hypoxic hypertensive rat pulmonary circulation. J. Cardiovasc. Pharmacol. 50, 697–702.

Huang, W., Delgado-West, D., Wu, J.T., Fung, Y.C., 2001. Tissue remodeling of rat pulmonary artery in hypoxic breathing. II. Course of change of mechanical properties. Ann. Biomed. Eng. 29, 552–562.

Humbert, M., Morrell, N.W., Archer, S.L., Stenmark, K.R., MacLean, M.R., Lang, I.M., Christman, B.W., Weir, E.K., Eickelberg, O., Voelkel, N.F., 2004. Cellular and molecular pathobiology of pulmonary arterial hypertension. J. Am. Coll. Cardiol. 43, S13–S24.

Humphrey, J., Eberth, J., Dye, W., Gleason, R., 2009. Fundamental role of axial stress in compensatory adaptations by arteries. J. Biomech. 42, 1–8.

Humphrey, J.D., 2013. Cardiovascular Solid Mechanics: Cells, Tissues, and Organs. Springer Science & Business Media.

Jiao, Y., Li, G., Korneva, A., Caulk, A.W., Qin, L., Bersi, M.R., Li, Q., Li, W., Mecham, R.P., Humphrey, J.D., 2017. Deficient circumferential growth is the primary determinant of aortic obstruction attributable to partial elastin deficiency. Arteriosclerosis, Thrombosis, Vascular Biol, ATVBAHA 117, 309079.

Kobs, R.W., Muvarak, N.E., Eickhoff, J.C., Chesler, N.C., 2005. Linked mechanical and biological aspects of remodeling in mouse pulmonary arteries with hypoxia-induced hypertension. Am. J. Physiol.-Heart Circulatory Physiol. 288, H1209–H1217.

Langleben, D., Szarek, J., Coflesky, J., Jones, R.C., Reid, L., Evans, J., 1988. Altered artery mechanics and structure in monocrotaline pulmonary hypertension. J. Appl. Physiol. 65, 2326–2331.

Le, V.P., Yamashiro, Y., Yanagisawa, H., Wagenseil, J.E., 2014. Measuring, reversing, and modeling the mechanical changes due to the absence of Fibulin-4 in mouse arteries. Biomech. Model. Mechanobiol. 13, 1081–1095.

Lee, Y., Naito, Y., Kurobe, H., Breuer, C., Humphrey, J., 2013. Biaxial mechanical properties of the inferior vena cava in C57BL/6 and CB-17 SCID/bg mice. J. Biomech. 46, 2277–2282.

Murtada, S.-I., Ferruzzi, J., Yanagisawa, H., Humphrey, J., 2016. Reduced biaxial contractility in the descending thoracic aorta of fibulin-5 deficient mice. J. Biomech. Eng. 138, 051008.

Murtada, S.-I., Humphrey, J.D., Holzapfel, G.A., 2017. Multiscale and multiaxial mechanics of vascular smooth muscle. Biophys. J. 113, 714–727.

Phillips, E.H., Di Achille, P., Bersi, M.R., Humphrey, J.D., Goergen, C.J., 2017. Multi-modality imaging enables detailed hemodynamic simulations in dissecting aneurysms in mice. IEEE Trans. Med. Imaging 36, 1297–1305.

Pursell, E.R., Vélez-Rendón, D., Valdez-Jasso, D., 2016. Biaxial properties of the left and right pulmonary arteries in a monocrotaline rat animal model of pulmonary arterial hypertension. J. Biomech. Eng. 138, 111004.

Qureshi, M.U., Colebank, M.J., Paun, L.M., Fix, L.E., Chesler, N., Haider, M.A., Hill, N.A., Husmeier, D., Olufsen, M.S., 2018. Hemodynamic assessment of pulmonary hypertension in mice: a model-based analysis of the disease mechanism. Biomech. Model. Mechanobiol., 1–25

Rahman, A., Davis, B., Lövdahl, C., Hanumaiah, V.T., Feil, R., Brakebusch, C., Arner, A., 2014. The small GTPase Rac1 is required for smooth muscle contraction. J. Physiol. 592, 915–926.

Ramachandra, A.B., Humphrey, J.D., Marsden, A.L., 2017. Gradual loading ameliorates maladaptation in computational simulations of vein graft growth and remodelling. J. R. Soc. Interface 14, 20160995.

Razavi, H., Zarafshar, S.Y., Sawada, H., Taylor, C.A., Feinstein, J.A., 2011. Quantitative characterization of postnatal growth trends in proximal pulmonary arteries in rats by phase-contrast magnetic resonance imaging. Am. J. Physiol-Lung Cellular Mol. Physiol. 301, L368–L379.

Rosenzweig, E.B., Kerstein, D., Barst, R.J., 1999. Long-term prostacyclin for pulmonary hypertension with associated congenital heart defects. Circulation 99, 1858–1865.

Schroeder, F., Polzer, S., Slažanský, M., Man, V., Skácel, P., 2018. Predictive capabilities of various constitutive models for arterial tissue. J. Mech. Behav. Biomed. Mater. 78, 369–380.

Siehr, S.L., Feinstein, J.A., Yang, W., Peng, L.F., Ogawa, M.T., Ramamoorthy, C., 2016. Hemodynamic effects of phenylephrine, vasopressin, and epinephrine in children with pulmonary hypertension: a pilot study. Pediat. Crit. Care Med. 17, 428–437.

Stenmark, K.R., McMurtry, I.F., 2005. Vascular Remodeling versus Vasoconstriction in Chronic Hypoxic Pulmonary Hypertension: A Time for Reappraisal? Am Heart Assoc.

Stenmark, K.R., Meyrick, B., Galie, N., Mooi, W.J., McMurtry, I.F., 2009. Animal models of pulmonary arterial hypertension: the hope for etiological discovery and pharmacological cure. Am. J. Physiol.-Lung Cellular Mol. Physiol. 297, L1013–L1032.

Sutliff, R.L., Walp, E.R., Kim, Y.H., Walker, L.A., El-Ali, A.M., Ma, J., Bonsall, R., Ramosevac, S., Eaton, D.C., Verlander, J.W., 2014. Contractile force is enhanced in aortas from pendrin null mice due to stimulation of angiotensin II-dependent signaling. PloS One 9, e105101.

Sutton, M., Ke, X., Lessner, S., Goldbach, M., Yost, M., Zhao, F., Schreier, H., 2008. Strain field measurements on mouse carotid arteries using microscopic three-dimensional digital image correlation. J. Biomed. Mater. Res. Part A: Off. J. Soc. Biomater., Jpn. Soc. Biomater., Aust. Soc. Biomater. Korean Soc. Biomater. 84, 178–190.

Tojais, N.F., Cao, A., Lai, Y.-J., Wang, L., Chen, P.-I., Alcazar, M.A.A., de Jesus Perez, V., Hopper, R.K., Rhodes, C.J., Bill, M.A., 2017. Codependence of bone morphogenetic protein receptor 2 and transforming growth factor-β in elastic fiber assembly and its perturbation in pulmonary arterial hypertension. Arteriosclerosis, Thrombosis, Vascular Biol., ATVBAHA 117, 309696.

Valentín, A., Cardamone, L., Baek, S., Humphrey, J., 2009. Complementary vasoactivity and matrix remodelling in arterial adaptations to altered flow and pressure. J. R. Soc. Interface 6, 293–306.

van Loon, P., Klip, W., Bradley, E., 1977. Length–force and volume–pressure relationships of arteries. Biorheology 14, 181–201.

Wang, Z., Chesler, N.C., 2012. Role of collagen content and cross-linking in large pulmonary arterial stiffening after chronic hypoxia. Biomech. Model. Mechanobiol. 11, 279–289.

Wang, Z., Lakes, R.S., Eickhoff, J.C., Chesler, N.C., 2013. Effects of collagen deposition on passive and active mechanical properties of large pulmonary arteries in hypoxic pulmonary hypertension. Biomech. Model. Mechanobiol. 12, 1115–1125.

Weizsäcker, H.W., Lambert, H., Pascale, K., 1983. Analysis of the passive mechanical properties of rat carotid arteries. J. Biomech. 16, 703–715.

Yoshibayashi, M., Nishioka, K., Nakao, K., Saito, Y., Matsumura, M., Ueda, T., Temma, S., Shirakami, G., Imura, H., Mikawa, H., 1991. Plasma endothelin concentrations in patients with pulmonary hypertension associated with congenital heart defects. Evidence for increased production of endothelin in pulmonary circulation. Circulation 84, 2280–2285.

Zeinali-Davarani, S., Choi, J., Baek, S., 2009. On parameter estimation for biaxial mechanical behavior of arteries. J. Biomech. 42, 524–530.